RSC Advances

PAPER

View Article Online
View Journal | View Issue

Check for updates

Cite this: *RSC Adv.*, 2026, **16**, 14170

Spectrophotometric detection of Fe^{3+} ions using garlic-derived alliin and bovine serum albumin-stabilized AgNPs

Rintumoni Paw, [abc] Palash J. Thakuria,[d] Ankur K. Guha *[d] and Chandan Tamuly *[ab]

Iron (Fe) is essential for biological systems, with ferric (Fe^{3+}) and ferrous (Fe^{2+}) states possessing biological significance. Imbalances in Fe^{3+} levels can lead to major health concerns. It necessitates accurate and specific detection of Fe^{3+} in drinking water sources. This study offers an eco-friendly, cost-effective colorimetric nanosensor for Fe^{3+} detection using silver nanoparticles (AgNPs) synthesized from garlic-derived alliin and bovine serum albumin (BSA). The nanoparticles were studied using UV-visible spectroscopy, X-ray photoelectron spectroscopy (XPS), X-ray diffraction (XRD), scanning electron microscopy (SEM), transmission electron microscopy (TEM) and energy dispersive X-ray spectroscopy (EDS). The AgNPs exhibited a plasmonic peak at 420 nm and TEM revealed spherical particles with an average diameter of 12.17 ± 0.60 nm. XPS analysis validated the binding energies of S 2p, C 1s, Ag 3d, N 1s, and O 1s. XRD showed that the AgNPs have a face-centered cubic (FCC) structure. The sensor has a detection limit of 5.54 fM for Fe^{3+}, with the highest sensitivity at pH 4 (68.80 ± 1.05% relative activity). Kinetic analysis indicated that zero-order kinetics provided the best fit under the given conditions. Computational modelling indicates a stable Fe^{3+} interaction with the NH group of BSA's histidine and the CHO group of alliin, with a binding energy of 16.1 kcal mol^{-1}. This supports the formation of a stable Ag-alliin-Fe complex. The sensor effectively detects Fe^{3+} in real water samples, underscoring its practical potential for environmental monitoring.

Received 16th November 2025
Accepted 3rd March 2026

DOI: 10.1039/d5ra08842a

rsc.li/rsc-advances

Open Access Article. Published on 16 March 2026. Downloaded on 5/23/2026 8:44:04 PM.
This article is licensed under a Creative Commons Attribution-NonCommercial 3.0 Unported Licence.

1. Introduction

Iron stands out for its high abundance among earth's crustal elements. It plays a pivotal role in various biological processes. It commonly occurs within the range of 0.5 to 50 mg L^{-1} in freshwater sources. Fe^{2+} (ferrous) and Fe^{3+} (ferric) are the two key redox states of iron relevant to biological systems. Ferric iron is integral to numerous physiological functions, including mitochondrial respiration, DNA synthesis and cellular signalling. It is a key component of cytochromes and iron-sulfur cluster proteins involved in electron transport and enzymatic activities.[2] However, both deficiency and excess of Fe^{3+} can lead to severe health issues. Iron deficiency is a leading cause of anaemia, while iron overload can result in conditions like hemochromatosis, diabetes, liver damage, neurodegenerative diseases such as Parkinson's and Alzheimer's and even cancer.[3] Estimates of the minimal daily iron requirement vary depending on age, gender, physiological state, and iron bioavailability, ranging from 10 to 50 mg per day. It has also been stated that drinking water with an iron level of approximately 2 mg L^{-1} poses no health risk.[1] The US EPA has established the maximum contamination threshold for iron in drinking water at 0.3 mg L^{-1} (approx. 5.4 μM).[4] The Joint FAO/WHO Expert Committee on Food Additives (JECFA) set a provisional maximum tolerable daily intake (PMTDI) of 0.8 mg per kilogram of body weight in 1983 to prevent excessive iron accumulation in the body. This limit applies to iron from all sources, excluding iron oxides used as colorants and iron supplements administered during pregnancy, lactation or for medical purposes.[1] Therefore, accurate and sensitive detection of Fe^{3+} in environmental and biological samples is crucial as a precautionary measure.

Heavy metal pollution has become a global issue since the industrial revolution. Paper manufacture, insecticides, tanning, metal plating, and mining all emit heavy metals into the environment, including Zn, Fe, Cu, Pb, Ni, Cd, and Hg. These are non-biodegradable and can build up in living things. So, these metals can cause a variety of health and environmental risks even at low quantities. Fe^{3+} is especially important among these because it is both a necessary food and a possible poison.[5] Various analytical methods have been developed for detecting

[a]*Natural Product Chemistry Section, CSIR-North East Institute of Science and Technology, Itanagar, Arunachal Pradesh-791110, India. E-mail: c.tamuly@gmail.com*
[b]*Academy of Scientific and Innovative Research (AcSIR), Ghaziabad-201002, India*
[c]*Dept of Chemistry, Silapathar Science College, Silapathar, Assam-787059, India*
[d]*Dept of Chemistry, Cotton University, Guwahati, Assam-781001, India. E-mail: ankurkantiguha@gmail.com*

© 2026 The Author(s). Published by the Royal Society of Chemistry

Open Access Article. Published on 16 March 2026. Downloaded on 5/23/2026 8:44:04 PM. This article is licensed under a Creative Commons Attribution-NonCommercial 3.0 Unported Licence.

Fe^{3+}, including atomic absorption spectroscopy, mass spectrometry, electrochemical techniques, fluorescence spectroscopy and colorimetry. The colorimetric techniques are getting popularity among these because of their ease of use, quick reaction times, affordability and capacity for on-site detection without the use of complex equipment. The most frequent basis for these techniques is the distinctive optical characteristics of nanoparticles, especially their surface plasmon resonance (SPR), which causes discernible colour changes upon interaction with target analytes.[6]

Many studies have been focused on the sensitive and selective detection of Fe^{3+} ions. These include fluorescent sensors like 1-naphthylamine derivatives,[7] L-cysteine capped Fe_3O_4@-ZnO core–shell nanoprobe,[8] carbon dot fluorescent probe obtained from the corn stalk powder by pyrolysis and microwave process,[9] L-glutathione stabilized red fluorescent gold nanoclusters.[10] Ye *et al.* observed that Fe^{3+} ions caused a gradual quenching of fluorescence in SiNPs, which was partially reversed by F^- ions due to the formation of a stable, colourless $FeCl_3$ compound.[11] Likewise, Kang *et al.* developed a fluorescent probe based on amino-functionalized Graphene Quantum Dots (FGQDs) for the efficient detection of Fe^{3+} using polypyrrole (PPy) both as a precursor (amine N) and as a surfactant.[12] Liu *et al.*[13] developed a fluorescent rhodamine B-functionalized chitosan nanoparticles, Golshan *et al.*[14] used Rhodamine B-modified nanocrystalline cellulose as fluorescent sensor for Fe^{3+} ion detection. Shellaih *et al.*[15] used luminescent nanodiamond-rhodamine conjugate for the selective "turn off" detection of Fe^{3+}. Rajam and Mahalakshmy[16] developed a dual-mode chemosensor, based on modified curcumin, capable of detecting Fe^{3+} ions through both colorimetric and fluorescence responses.

The AgNPs based colorimetric detection include AgNPs-citrate-glutathione,[17] AgNPs synthesized using orchid tree (*Bauhinia variegata*) leaf.[18] In addition to colorimetry, Ma *et al.* used AgNPs on well-ordered TiO_2 nanotube arrays for iron ion sensing performed with the anodic stripping voltammetry method.[19] AgNPs synthesized using polyvinyl alcohol (PVA) and sodium chloride (NaCl),[20] AgNPs synthesized using *Syzygium cumini* fruit extract,[21] chitosan capped AgNPs,[22] *N*-acetyl-L-cysteine-stabilized AgNPs[23] were also used for the colorimetric detection of Fe^{3+} ions. Likewise, AuNPs synthesized using the aqueous extract of *Eleutherine bulbosa* leaf,[24] glycol-chitosan AuNPs,[25] AuNPs capped with *ortho*-hydroxybenzoic acid (*o*-HBA AuNPs),[26] AuNPs prepared using *Hibiscus cannabinus* leaf extract,[27] AuNPs functionalized with mercaptosuccinic acid[28] were used for colorimetric detection of Fe^{3+}. Some other colorimetric sensors include sulfasalazine (SSZ) functionalized microgels (SSZ-MGs),[29] Alizarin Red S (ARS) reagent,[30] bis(1,2,3-triazolyl-γ-propyltriethoxysilane) functionalized with a Schiff base-chalcone moiety,[31] *Terminalia chebula* extract.[32]

From these, evident that the colorimetric techniques have gained attention due to their simplicity, speed, sensitivity, selectivity and ease of use making them suitable for point-of-care applications.[33] Out of these, AgNps are considered highly advantageous among noble nanoparticles due to their low cost, stability, non-toxicity and excellent conductivity. Their wide absorption range makes them ideal for applications such as colorimetric sensors, enabling the naked-eye detection of various target analytes. The plant-mediated synthesis of AgNPs is a promising, cost-effective, one-step, non-toxic and eco-friendly method.[34] Despite these advantages, there are few publications on the use of AgNPs as probes for colorimetric sensing of Fe^{3+}. Recent research has demonstrated that proteins can interact with nanomaterials by altering their optical characteristics. Albumin belongs to the class of water-soluble globular proteins. A serum albumin derived from cattle (bovine), commonly referred to as BSA can interact and change its conformational state on the surface of metal nanoparticles, modifying their optical characteristics, which can be directly observed by spectrophotometry. Proteins' ability to affect the optical characteristics of silver nanoparticles has sparked interest in their prospective application in colorimetry.[35]

Garlic (*Allium sativum*) is one of the most well studied spices which is used both as a food and as a therapeutic agent. In many cultures' folklore, it is regarded as a powerful preventative and therapeutic medicinal substance. It contains a range of sulfur-containing bioactive molecules—such as alliin, allicin, ajoenes, vinyldithiins, flavonoid compounds like quercetin, with an abundance of *S*-allyl mercapto cysteine and glucose in the aqueous extract, which may play an important role in NP production by contributing to the capping and stabilising processes. As a result, garlic extract can be employed as a facilitating agent for NP synthesis, with allicin and other carbohydrates serving as the key stabilising moieties.[36,37]

The current study seeks to design a nanosensor that detects Fe^{3+} ions in aqueous solutions with selectivity, precision, low detection limits and an eco-friendly synthesis approach. It investigates the usage of AgNPS synthesised from bovine serum albumin (BSA) and garlic extract. To reduce costs and technological constraints, spectrophotometric technique that relied on surface plasmon resonance was adopted for the nanosensor.

2. Materials and methods

2.1 Materials

Garlic was collected from the local market, Naharlagun (27.1030°N, 93.7008°E; 155 m asl) in Arunachal Pradesh, India. All chemicals of analytical standard were procured from Sigma-Aldrich. The chemicals used include $AgNO_3$ (99.99%), $BaCl_2 \cdot 2H_2O$ (99%), $CaCl_2$, $Al_2(SO_4)_3$, $CrCl_3$ (99.9%), $CoCl_2 \cdot H_2O$ (97%), $NiCl_2 \cdot 6H_2O$ (98%), $CuSO_4$, $ZnSO_4 \cdot 7H_2O$ (99.10%), $FeCl_3$, $FeSO_4 \cdot 7H_2O$, and BSA.

2.2 Preparation of garlic extract and synthesis of BSA-alliin-Ag NPs

Cloves from five garlics were peeled and ground to a fine paste using a mortar and pestle. Garlic paste was added to deionized water in a 1 : 10 (w/v) proportion and stirred magnetically at 60 °C for 45 minutes. Afterward, the mixture was allowed to cool to ambient temperature (24–25 °C) and was filtered using Whatman filter paper with a pore size of 20–25 μm. The resulting

Open Access Article. Published on 16 March 2026. Downloaded on 5/23/2026 8:44:04 PM. This article is licensed under a Creative Commons Attribution-NonCommercial 3.0 Unported Licence.

filtrate, referred to as garlic extract, was used for subsequent analyses.[36]

The AgNPs were synthesized by reducing Ag^+ ions from 200 mL $AgNO_3$ using 20 mL of the prepared aqueous garlic extract, which contains alliin as the active compound (brown coloration observed).[36] Subsequently, 10 μl 0.1% BSA was added to the suspension of 10 mL AgNPs and mixed using stirrer, resulting in a dark brown-coloured solution.

2.3 Characterization of the synthesized nanoparticles

Characterization of the synthesized nanoparticles was done using UV-visible spectroscopy, X-ray photoelectron spectroscopy (XPS), X-ray diffraction (XRD), scanning and transmission electron microscopy (SEM and TEM), and TEM-Energy dispersive X-ray spectroscopy (EDS). A Lambda 25 spectrophotometer (PerkinElmer, Switzerland) was used to record UV-visible absorption spectra in the 300–800 nm range in order to track the synthesis of AgNPs. A Bruker D8 Advance X-ray diffractometer, employing Cu Kα radiation ($\lambda = 0.15405$ nm), was used for XRD analysis with a scanning speed of 3° min^{-1}. To analyze nanoparticle surface features, a Sigma 300 VP FE-SEM was employed, offering 1.2 nm resolution at an accelerating voltage of 15 kV. High-resolution TEM pictures were acquired using a JEM-2100 (JEOL Ltd, Japan) with a 200 kV accelerating voltage. XPS was performed utilising a Thermo Scientific ESCALAB Xi^+ equipment to ascertain the elemental composition, empirical formula, and chemical and electronic states of the constituent elements. Based on the TEM picture, ImageJ software was used to measure the nanoparticles' size. The elemental composition of the nanoparticles was determined using Aztec (Oxford Instruments, UK) were used to characterise the synthesised nanoparticles.

2.4 Sensitivity of BSA-alliin-AgNPs for detection of Fe^{3+} ions

The surface plasmon resonance (SPR) band was observed to assess the reaction of the synthesised BSA-alliin-AgNPs to different metal ions, specifically Ba^{2+}, Ca^{2+}, Al^{3+}, Cr^{3+}, Co^{2+}, Ni^{2+}, Cu^{2+}, Zn^{2+} and Fe^{3+}. Standard solutions of each metal ion were prepared in deionized water at a concentration of 1 mM. A solution of 5 mL of diluted BSA-alliin-AgNPs in water was supplemented with 0.2 mL of 1 mM salt solution of each metal ion solution. The mixture was shaken using vortex for 2 minutes at room temperature to allow for interaction between the nanoparticles and the metal ions. Changes in colour of the solution was recorded visually and the absorbance spectra of the mixtures were recorded using a UV-vis spectrophotometer across the wavelength range of 300–800 nm. The specific absorbance peak corresponding to the surface plasmon resonance (SPR) band of BSA-alliin-AgNPs was monitored to observe any shifts or intensity changes indicative of metal ion interaction.

To assess the limit of detection (LoD) for Fe^{3+} ion sensing, 10–120 μl of 01 nM $FeCl_3$ solution (2–16 fM) was added separately to 400 μl of the synthesised BSA-alliin-AgNPs solution. The resulting solution's absorbance maxima were measured at 420 nm. A linear calibration curve was plotted to determine the lowest detectable concentration of Fe^{3+} and the LoD and LoQ were computed using the eqn (1) and (2), based on the slope and the response standard deviation.[38]

$$\text{LoD} = 3.3 \times \text{SD}/S \quad (1)$$

$$\text{LoQ} = 10 \times \text{SD}/S \quad (2)$$

where SD = standard deviation of absorbance maxima of the control ($N = 8$), S = slope of the calibration curve.

2.5 Real sample analysis

Six water samples were obtained from tube-wells of three sites—Lekhi, Doimukh and Naharlagun, located in Arunachal Pradesh within the geographical range of 27.06–27.14°N latitude and 93.41–93.78°E longitude, at elevations between 200 and 283 meters. The water samples were tested using the methods described above. A solution of 3 mL of diluted BSA-alliin-AgNPs in water was supplemented with 0.2 mL of the sample water. The mixture was shaken using vortex for 2 minutes at room temperature to allow for interaction between the nanoparticles and the metal ions. The absorbance spectra of the mixtures were recorded using a UV-vis spectrophotometer across the wavelength range of 300–800 nm. The quantity of Fe^{3+} in the samples was estimated using the standard linear regression model derived based on the absorbance maxima and the concentration of Fe^{3+} solution.

2.6 Optimization of pH and reaction kinetics between BSA-alliin-Ag NPs and Fe^{3+}

The impact of pH on Fe^{3+} detection with synthesised AgNPs has been investigated at room temperature, using the absorbance peak in the presence of Fe^{3+}. For this, the absorbance spectra of 3 mL diluted BSA-alliin-AgNPs were recorded at pH 2, 4, 6 and 8 maintained using buffer tablet at room temperature (25 °C). The relative activity percentage was calculated and plotted against their respective changes to optimize the process using the following equation (eqn (3)):

$$\text{Relative activity (\%)} = A_c \times 100/\Sigma(A_m - A_c) \quad (3)$$

where A_c = the absorbance maxima of the BSA-alliin-AgNPs under the specified conditions, A_m = the highest absorbance maximum of BSA-alliin-AgNPs.

To study the kinetics of the interaction between BSA-alliin-Ag NPs and Fe^{3+}, 5 mL of the AgNPs was mixed with 25 μl of a 01 nM Fe^{3+} solution. The spectroscopic absorbance of the resulting mixture was measured every five minutes. In this study, we tested the linear kinetic models described in eqn (4)–(6).[39]

$$\text{Zero order: } [A_t] = [A_0] - k_0 t \quad (4)$$

$$\text{First order: } \ln([A_t]/[A_0]) = -k_1 t \quad (5)$$

$$\text{Second order: } 1/[A_t] = k_2 t + 1/[A_0] \quad (6)$$

© 2026 The Author(s). Published by the Royal Society of Chemistry

Open Access Article. Published on 16 March 2026. Downloaded on 5/23/2026 8:44:04 PM. This article is licensed under a Creative Commons Attribution-NonCommercial 3.0 Unported Licence.

The peak absorbance at time t is indicated by $[A_t]$ in these equations, and the peak absorbance at $t = 0$ is indicated by $[A_0]$. The zero, first, and second order rate constants are denoted by the constants k_0, k_1, and k_2, respectively. Charting $[A_t]$ against T, $\ln([A_t]/[A_0])$ against T and $1/[A_t]$ against T, respectively, represents the kinetic models. The constants k_0, k_1, and k_2 were obtained from the slopes of the associated linear plots.

2.7 Computational details

To investigate the interaction between the silver atom and the alliin molecule, the geometry of the Ag doped alliin molecule was optimized at M06-2X/def2-TZVP level.[40] Harmonic vibrational frequency calculation confirms it to be local minimum. All calculations were performed using Gaussian 16 suite of program.[41]

3. Results and discussion

3.1 Formation of BSA-alliin-AgNPs

After adding the garlic extract, the colourless $AgNO_3$ solution turned brown indicating formation of alliin-AgNPs (Fig. 1A). However, alliin-AgNPs didn't show sensitivity towards Fe^{2+} and Fe^{3+} (Fig. 1B).[36] So, BSA-alliin-AgNPs have been prepared to study its selectivity and sensitivity towards various metal ions. The hue of the alliin-AgNPs darkens after the addition of BSA. It demonstrated the effect of garlic extract and BSA as a reducing agent to produce BSA-garlic extract-AgNPs. Previous investigations have observed a similar hue following the addition of alliin containing garlic extract to $AgNO_3$.[36] The production of AgNPs was suggested by bell-shaped spectra with absorbance peak at λ_{max} = 420 nm (Fig. 1). AgNPs have a UV-visible absorption maximum between 400–500 nm due to surface plasmon resonance.[42] The broad peak reflects the nanoparticles' scattered nature, whereas the single peak suggests their spherical shape.[43] Paw *et al.* identified alliin as a key molecule in the synthesis of AgNPs, which was validated by HPLC analysis.[36] Alliin is a sulfur-containing amino acid derivative. When garlic cloves are crushed, alliin is transformed into allicin, the chemical that gives fresh garlic its pungent scent. The enzyme allinase catalyses the conversion of alliin into allicin. Higher temperatures damage protein characteristics. So, boiling garlic removes allinase activity, resulting in reduced pungency. In the current investigation, the garlic paste was heated immediately after crushing to inactivate the enzyme and inhibit conversion of the targeted biocompound alliin to allicin.[36,44,45]

3.2 Scanning and transmission electron microscopy (SEM and TEM)

The scanning electron microscopy (SEM) demonstrates that the synthesised nanoparticles are very cohesive and have a non-homogeneous surface structure (Fig. 2A). This SEM image corresponds to the BSA-alliin-AgNPs in the solid state. The apparent aggregation observed in the SEM image is therefore likely influenced by biomolecule capping and sample drying effects during SEM preparation, and does not necessarily reflect the dispersion state of the nanoparticles in solution during sensing measurements. The Fe^{3+} sensing experiments were carried out in colloidal solution. The observed clustering could possibly be attributable to the interplay of bovine serum albumin (BSA) and alliin, which could function as both reducing and capping agents.[46,47] Bright-field transmission electron microscopy (TEM) indicates that BSA-alliin-AgNPs are primarily spherical, with a mean diameter of 12.17 ± 0.60 nm and most particles falling within the 10–15 nm range (Fig. 2B–D). This is strongly consistent with previously reported studies: Chemical reduction yielded AgNPs coupled to BSA with diameters ranging from 11–15 nm, as measured by TEM and Dynamic Light Scattering (DLS).[48] Gebregeorgis *et al.* reported that BSA-conjugated AgNPs typically measure 11–15 nm.[49] These results suggest that BSA effectively directs nanoparticle nucleation and development, resulting in a relatively narrow and homogeneous size distribution. The spherical shape and nanoscale size are appropriate for a variety of biomedical applications, increasing surface area and reactivity.[50] EDS was used to determine the chemical composition of the

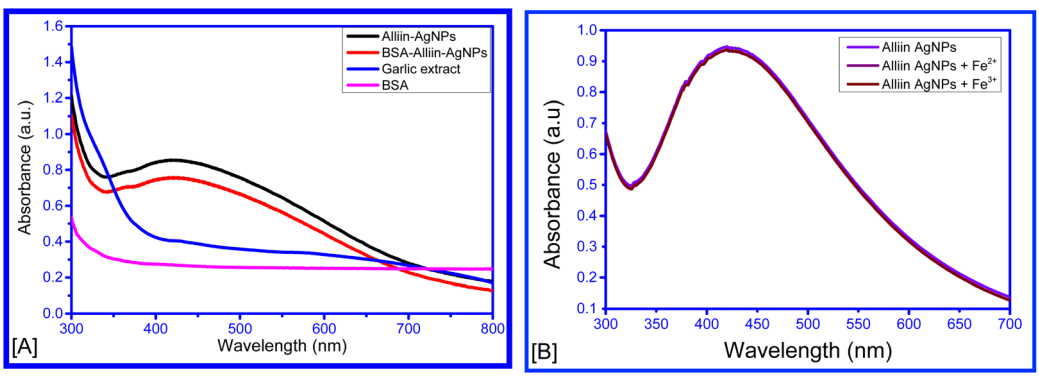

Fig. 1 (A) UV-visible absorption spectra of garlic extract (blue), BSA (pink), alliin-AgNPs (black), BSA-alliin-AgNPs (red) recorded in the wavelength range of 300–800 nm. The characteristic surface plasmon resonance (SPR) peak observed in the BSA-alliin-AgNPs spectrum confirms the formation of silver nanoparticles, while the BSA and garlic extract spectra show no such SPR peak. (B) Spectrophotometric response of alliin-AgNPs after addition of Fe^{2+} and Fe^{3+} ions. It didn't show significant changes in absorbance spectra.

Open Access Article. Published on 16 March 2026. Downloaded on 5/23/2026 8:44:04 PM.
This article is licensed under a Creative Commons Attribution-NonCommercial 3.0 Unported Licence.

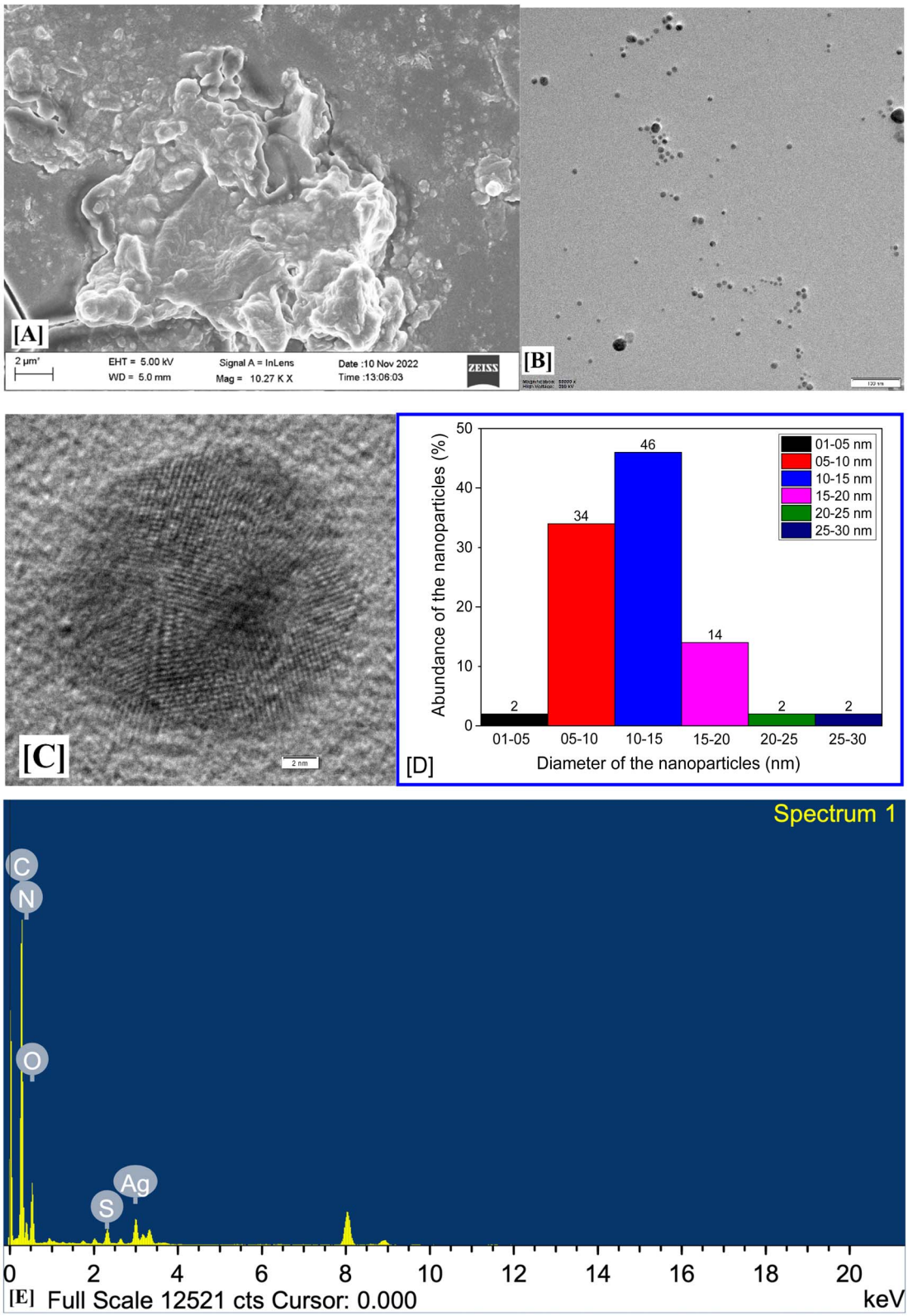

Fig. 2 (A) Scanning electron micrograph (SEM) showing the aggregated and irregular surface morphology of BSA-alliin-AgNPs, suggesting effective capping and stabilization by biomolecules. (B and C) Transmission electron micrographs (TEM) depicting the spherical shape and uniform dispersion of nanoparticles; image (C) highlights the crystalline nature of an individual nanoparticle with visible lattice fringes. (D) Histogram representing the size distribution of BSA-alliin-AgNPs, showing that the majority of nanoparticles range between 10–15 nm in diameter, (E) energy-dispersive X-ray spectrometry (EDS) spectrum of the synthesized nanoparticles that showed the presence of 71.36% C K, 6.48% N K, 9.43% O K, 2.10% S K, 10.63% Ag L, by weight.

© 2026 The Author(s). Published by the Royal Society of Chemistry

Open Access Article. Published on 16 March 2026. Downloaded on 5/23/2026 8:44:04 PM.
This article is licensed under a Creative Commons Attribution-NonCommercial 3.0 Unported Licence.

nanoparticle surface. As shown in Fig. 2(E) the nanoparticle surface contained 71.36% C K, 6.48% N K, 9.43% O K, 2.10% S K, 10.63% Ag L, by weight with atomic percentage of 83.00% C K, 6.47% N K, 8.24% O K, 0.91% S K, 1.38% Ag L.

3.3 X-ray photon spectroscopy and X-ray diffraction study

The XPS results indicated binding energy signatures for S 2p, C 1s, Ag 3d, N 1s, and O 1s (Fig. 3). The S 2p peak is divided into S $2p_{3/2}$ and S $2p_{1/2}$, with a spin–orbit splitting of around 1.2 eV. The S 2p binding energies of 167.7 eV and 167.9 eV suggest the presence of oxidised or covalently bonded sulphur species, with –S–S– (disulphide) being a possible option. It also represents sulphur under specific chemical conditions. This data envelope is fitted to a spin–orbit doublet (the S $2p_{3/2}$ and $2p_{1/2}$ peaks) at the right separation (1.2 eV).[51] Double peaks in the Ag 3d area indicate that metallic silver (Ag^0) is the main element, with binding energies of 367.65 eV for Ag^0 $3d_{5/2}$ and 373.65 eV for Ag^0 $3d_{3/2}$, indicating the presence of AgNPs (Fig. 3B). The N 1s binding energy of primary amine ($-NH_2$) ranges from 399.5 to 400.5 eV.[52] Thus, the binding energy peak at 399.55 eV indicated

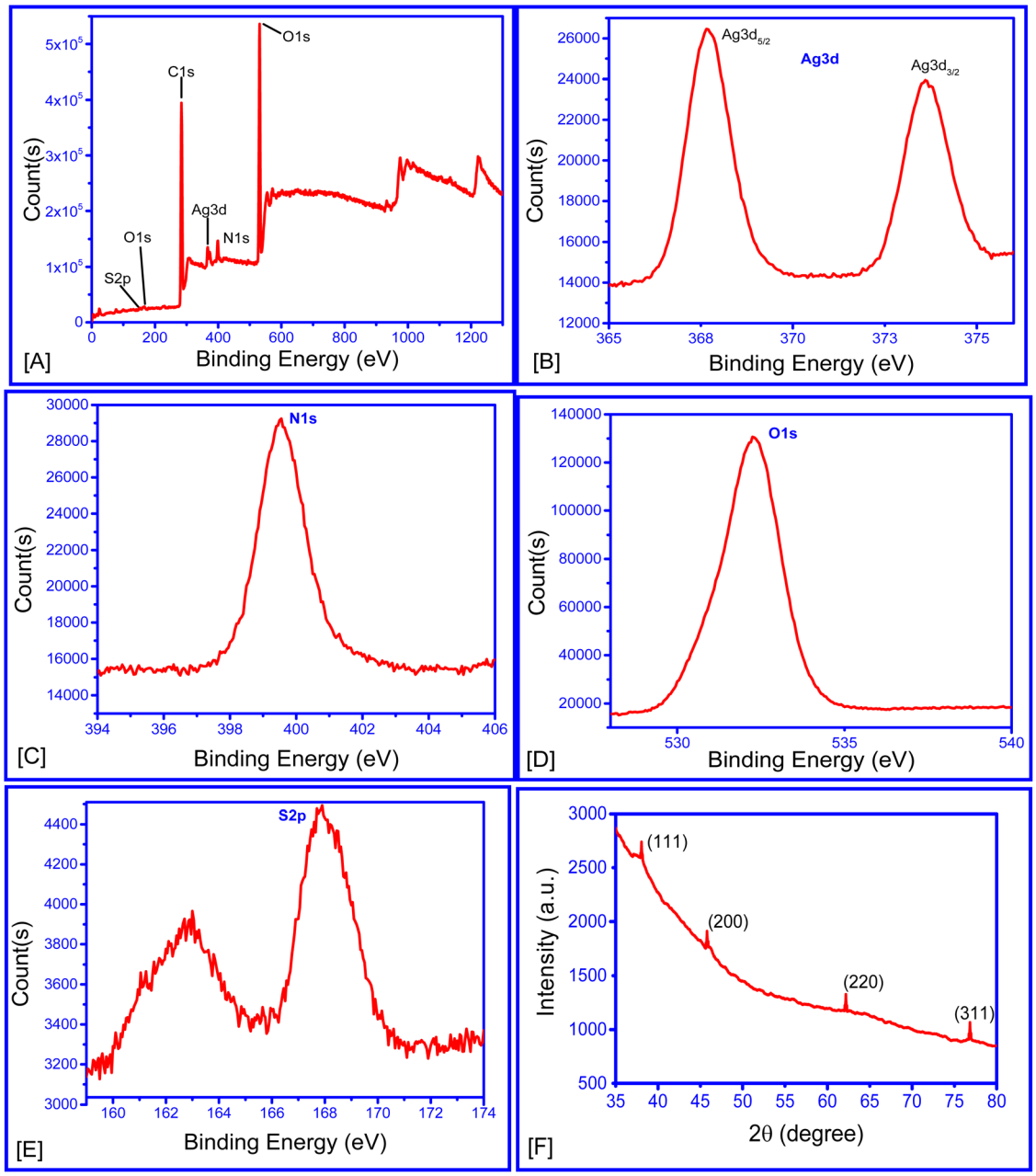

Fig. 3 (A) XPS survey scan of BSA-alliin-AgNPs revealing the presence of elements Ag, C, O, N, and S; (B–E) high-resolution XPS spectrum of (B) Ag 3d, showing Ag $3d_{5/2}$ and Ag $3d_{3/2}$ peaks, (C) N 1s, (D) O 1s, (D) C 1s, (E) S 2p; (F) X-ray diffraction (XRD) pattern of BSA-alliin-AgNPs showing characteristic peaks at $2\theta = 38.2°$, 44.4°, 64.5°, and 77.4°, corresponding to the (111), (200), (220) and (311) planes of the face-centered cubic (fcc) structuse.

Open Access Article. Published on 16 March 2026. Downloaded on 5/23/2026 8:44:04 PM.
This article is licensed under a Creative Commons Attribution-NonCommercial 3.0 Unported Licence.

the existence of the $-NH_2$ group. A binding energy peak for O 1s was detected at 532.25 eV in the O 1s XPS spectrum, which typically corresponds to –C–OH.[53]

Fig. 3F displays the XRD pattern of the synthesised BSA-alliin-AgNPs. The diffraction peaks at 38.06°, 45.8°, 62.62°, and 76.84° correspond to the (111), (200), (220), and (311) planes of the face-centered cubic (FCC) structure of Ag, respectively. Similar findings have been found for various AgNPs.[54]

3.4 Analytical performance in selectivity metal ions

BSA-alliin-AgNPs were systematically evaluated to study their selectivity and sensitivity towards various metal ions by introducing aqueous solutions of Ba^{2+}, Ca^{2+}, Al^{3+}, Cr^{3+}, Co^{2+}, Ni^{2+}, Cu^{2+}, Zn^{2+} and Fe^{3+} into the nanoparticle suspension. Notably, only the addition of Fe^{3+} ions resulted in a visible transformation of the solution's colour from brown to colourless, indicating a specific interaction between Fe^{3+} and the BSA-alliin-AgNPs. The noticeable colour change was further supported by a marked reduction in the surface plasmon resonance (SPR) absorbance peak of the nanoparticles, as illustrated in Fig. 4. Minimal spectral or visual changes were observed in the presence of other tested metal ions, indicating a strong specificity of the nanoparticles for Fe^{3+}. This selective response is likely due to the strong interaction between Fe^{3+} ions and functional groups on the nanoparticle surface, potentially involving redox processes or chelation. These properties highlight the potential of BSA-alliin-AgNPs for use in the colorimetric sensing of Fe^{3+} ions. When BSA forms a stabilizing layer on AgNPs, it maintains colour conditions.[55] In essence, the chemical properties of the iron ions disrupt the protective BSA layer and the electrostatic forces that keep the AgNPs dispersed, causing them to aggregate and lose their colloidal stability. The end result of the iron interactions is often a loss of colloidal stability, where individual nanoparticles stick together to form larger aggregates leading to lowering of the absorbance of UV-visible spectra.[55,56]

From the UV-visible spectral analysis presented in Fig. 4C, it is evident that the characteristic absorbance peak of BSA-alliin-AgNPs at 420 nm gradually decreases with the incremental addition of Fe^{3+} ions, indicating a concentration-dependent response. This observation suggests a strong interaction between Fe^{3+} and the nanoparticle system, likely resulting in

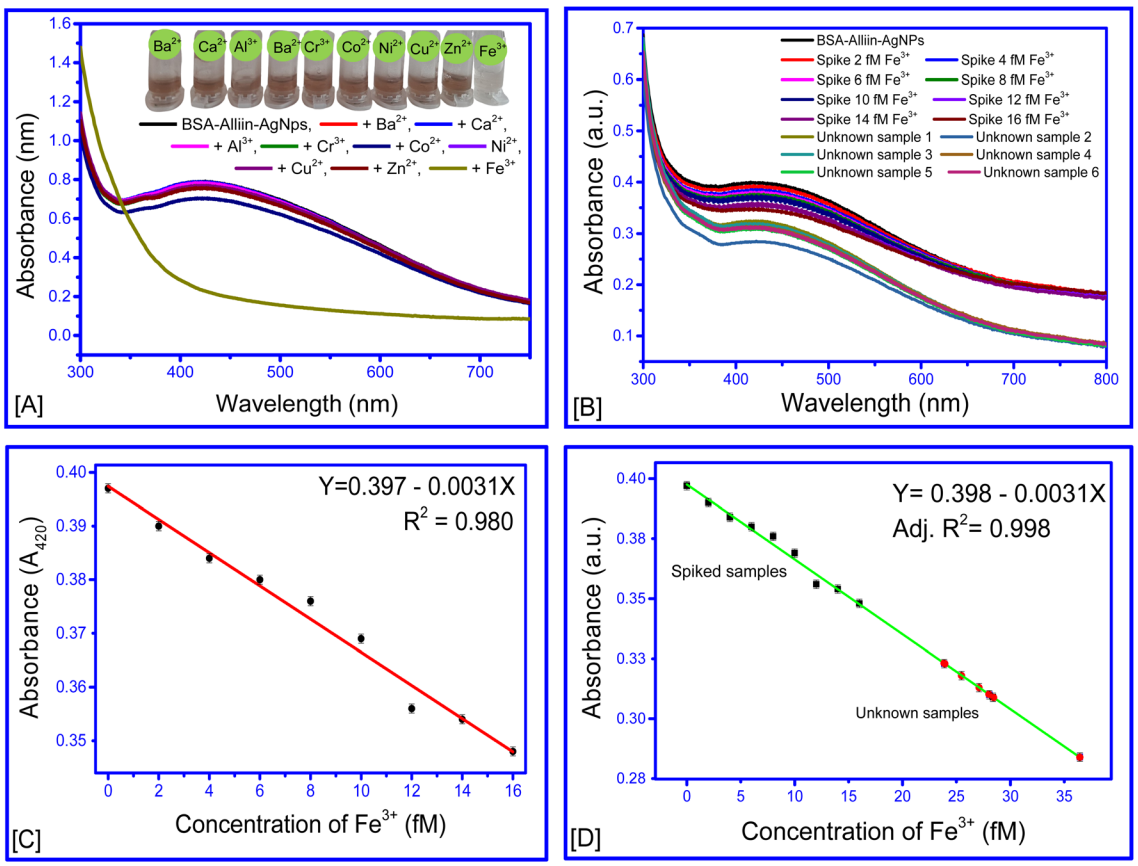

Fig. 4 (A) The UV-visible absorption spectra of BSA-alliin-AgNPs exposed to different metal ions (Ba^{2+}, Ca^{2+}, Al^{3+}, Cr^{3+}, Co^{2+}, Ni^{2+}, Cu^{2+}, Zn^{2+}, and Fe^{3+}), that revealed a unique and noticeable spectral response specifically for Fe^{3+}, (B) UV-visible spectra of BSA-alliin-AgNPs after addition of Fe^{3+} (2–16 fM) containing distilled water and after the addition of real water samples with unknown Fe^{3+} concentration (C) calibration plot of absorbance *versus* Fe^{3+} concentration indicating a linear correlation for quantitative detection ($N = 8$) for limit of detection (LoD) analysis, (D) calibration plot of absorbance *versus* Fe^{3+} concentration of Fe^{3+} spiked water samples and real water samples of with unknown Fe^{3+} concentration ($N = 8$).

© 2026 The Author(s). Published by the Royal Society of Chemistry

Open Access Article. Published on 16 March 2026. Downloaded on 5/23/2026 8:44:04 PM. This article is licensed under a Creative Commons Attribution-NonCommercial 3.0 Unported Licence.

aggregation or changes in surface plasmon resonance behaviour. Quantitative analysis (Fig. 4D) reveals a significant negative linear correlation between the absorbance intensity and Fe^{3+} concentration over the range of 2–16 fM, with a Pearson correlation coefficient of $r = -0.99$, confirming the sensitivity and reliability of the system.

The linear regression equation describing this relationship is:

$$Y = 0.397 - 0.0031X,$$

with a coefficient of determination

$$R^2 = 0.98,$$

where Y is the absorbance at 420 nm and X is the Fe^{3+} concentration in femtomolar (fM).

Based on this calibration, the limit of detection (LoD) for Fe^{3+} ions was calculated as 5.54 fM, and the limit of quantification (LoQ) as 16.78 fM using eqn (1) and (2) stated above, where SD = 0.0052 and slope = 0.0031. This LoD is significantly lower than those reported by many existing methods (Table 1), demonstrating the potential of BSA-alliin-AgNPs as an ultrasensitive spectrophotometric sensor for Fe^{3+} ion detection in environmental and biological samples. The reported calibration range of 2–16 fM of the proposed sensor was under optimized laboratory conditions. It was intentionally selected to demonstrate its lower detection limit and signal linearity at trace concentrations. However, the sensing platform is not intrinsically limited to this narrow concentration window. The range can be readily extended by adjusting the amount of the nanoparticles. The low relative standard deviation indicates that the present nanoparticles had consistent spectrophotometric responses, contributing to good reproducibility without requiring complex synthesis and complicated experimental conditions.

The analytical performance of the proposed method was assessed using Fe^{3+}-spiked samples and real samples with

Table 1 Comparison of sensing parameters for Fe^{3+} ion detection using fluorescence and colorimetric probes

S. no.	Sensor	Colour change after Fe^{3+} addition/principle	Absorbance considered	Calibration range	LoD
(A) Fluorescence probe					
1	L-Cysteine (L-Cys) capped Fe3O4@ZnO[8]	Fluorescence intensity quenched with increase of Fe^{3+}	The fluorescence intensity was recorded at 337 nm, with an excitation at 290 nm	0.01 to 133 μmol L^{-1}	3 nmol L^{-1}
2	Europium metal–organic framework[57]	Quenching mechanism for the fluorescence turn-off	Upon excitation at 320 nm, the emission spectra display a faint ligand-related band near 375 nm and a strong, broad emission peak centered around 430 nm	0.5–3.7 ppm	2.9 μM
3	Chitosan nanospheres-rhodamine B[13]	Quenching effect of Fe^{3+}	Excitation 505 nm, emission 590 nm	10^{-4}–10^{-2} mol L^{-1}	10^{-5} mol mL^{-1}
4	Carbon dot fluorescent probe[9]	Fluorescence quenching	Excitation wavelength of 365 nm, emission 380 nm to 600 nm	0 to 128 μM	63 nM
5	SiNP[11]	Fluorescence quenching	Excitation 370 nm and emission 462	0 to 100 μmol L^{-1}	0.05 μmol L^{-1}
6	Functionalized graphene quantum dots using PLA process[12]	Fluorescence quenching	Excitation 360 nm, emission 260 and 360 nm	500 nM to 50 μM	0.5 μM
(B) Colorimetric probe					
7	AgNPs from orchid tree (*Bauhinia variegata*) leaf extract[18]	Yellow to brown	430 nm	6–100 μM	2.08×10^{-6} M
8	*Terminalia chebula* extract[32]	Pale yellow to blue	576 nm	0–150 μM	60.8 μM
9	$P_2O_7^{4-}$ AuNPs[58]	Pink to blue	A_{750nm}/A_{535nm}	10 and 60 μM	5.6 μM
10	Ag/AgCl NPs by fruit extract of *Syzygium cumini*[21]	Yellow to pink	500 nm	10.0 to 100.0 μM	1.2 μM
11	*N*-Acetyl-L-cysteine-stabilized silver nanoparticles[23]	Brown to colourless	400 nm	80 nM to 80 μM	80 nM
12	AuNPs conjugated with glycol chitosan[25]	Light red to dark midnight blue	A_{700nm}/A_{510nm}	0–180 μM	11.3 nM
13	Mercaptosuccinic acid-capped AuNPs[28]	Red to blue	A_{530nm}/A_{660nm}	20–30 ng mL^{-1}	23 ng mL^{-1}
14	Sulfasalazine (SSZ) functionalized microgels[29]	Light-yellow to orange	A_{485nm}/A_{362nm}	0–12 μM	0.110 μM
15	BSA-alliin AgNPs (present study)	Brown to colourless	420 nm	02–16 fM	5.54 fM

Open Access Article. Published on 16 March 2026. Downloaded on 5/23/2026 8:44:04 PM.
This article is licensed under a Creative Commons Attribution-NonCommercial 3.0 Unported Licence.

Table 2 Analytical performance of the proposed method for determination of Fe^{3+} in spiked samples and real samples with unknown concentration of Fe^{3+}

S. no.	Spiked Fe^{3+} (fM)	Fe^{3+} detected (fM)	RSD (%) ($N = 8$)	Recovery %
1	2	1.81 ± 0.30	16.29	90.73
2	4	4.23 ± 0.32	7.55	105.85
3	6	5.85 ± 0.27	4.60	97.45
4	8	7.10 ± 0.30	4.21	88.71
5	10	8.95 ± 1.06	11.83	89.52
6	12	13.32 ± 0.49	3.69	110.22
7	14	13.27 ± 0.97	7.29	94.76
8	16	16.33 ± 0.34	2.10	102.07
9	Sample 1	23.71 ± 0.17	0.73	—
10	Sample 2	36.41 ± 0.11	0.31	—
11	Sample 3	25.36 ± 0.17	0.66	—
12	Sample 4	27.14 ± 0.21	0.76	—
13	Sample 5	28.55 ± 0.17	0.60	—

unknown Fe^{3+} concentrations (Table 2). For spiked concentrations between 2 and 16 fM, the detected Fe^{3+} values were in good agreement with the added amounts. The method exhibited acceptable precision, with relative standard deviation (RSD, $N = 8$) values ranging from 2.10% to 16.29%. Recovery values between 88.71% and 110.22% confirmed the good accuracy of the method over the investigated concentration range. Application of the method to real samples resulted in Fe^{3+} concentrations from 23.71 ± 0.17 to 36.41 ± 0.11 fM, accompanied by low RSD values (0.31–0.76%), demonstrating excellent reproducibility and practical applicability for trace-level Fe^{3+} analysis.

3.5 Optimization of pH for Fe^{3+} ion detection

The sensitivity of BSA-alliin-AgNPs towards Fe^{3+} ions was evaluated under varying pH conditions (2, 4, 6 and 8) to determine the optimal environment for colorimetric sensing. These pH points were selected to provide an initial assessment of sensor performance across acidic to mildly basic conditions, rather than to establish detailed pH-dependent behaviour. UV-visible absorption spectra (Fig. 5A and B) revealed that the presence of Fe^{3+} ions consistently led to a decrease in the characteristic peak absorbance of the nanoparticle solution, indicative of nanoparticle aggregation or structural modification upon interaction with Fe^{3+}. Among the tested pH values, the most pronounced decrease in absorbance was observed at pH 4, corresponding to a relative activity of 68.80 ± 1.05%, thereby signifying the most effective interaction between Fe^{3+} and the functionalized nanoparticles under mildly acidic conditions. This response is likely influenced by the protonation of functional groups present on the nanoparticle surface, particularly those from BSA and alliin, which may facilitate stronger

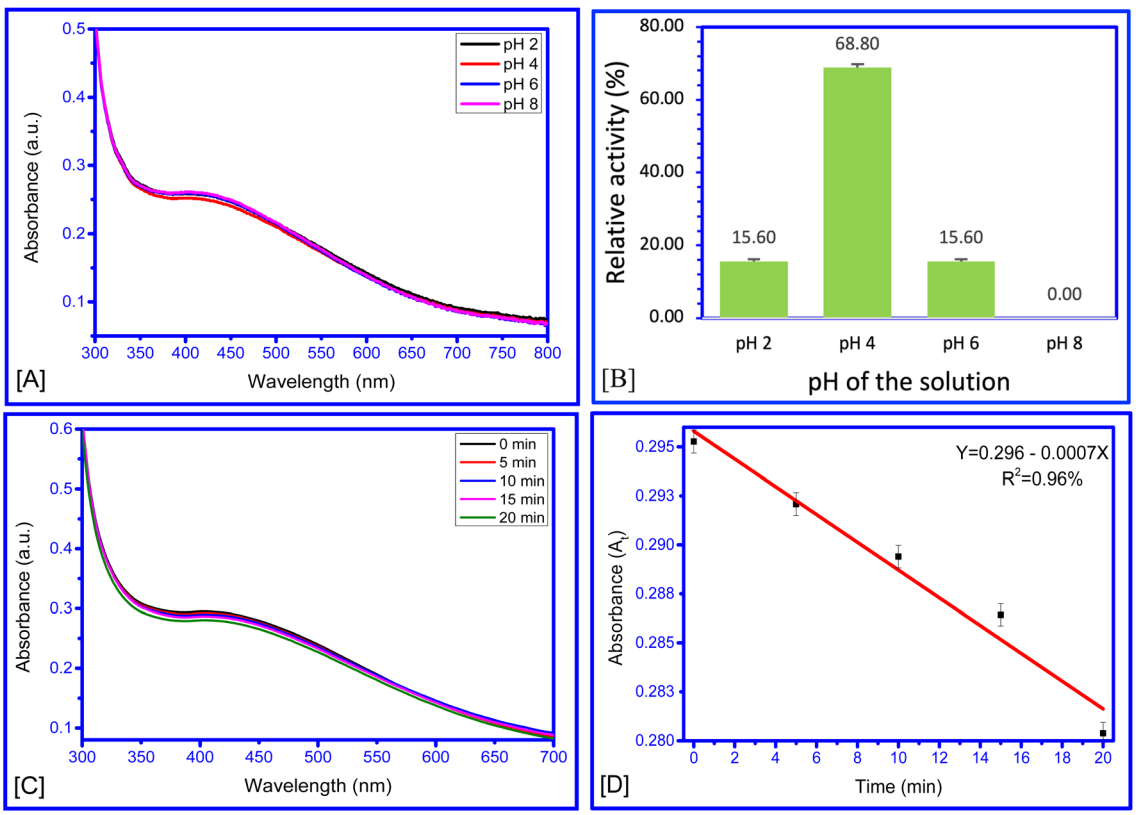

Fig. 5 (A and B) UV-visible spectra of the BSA-alliin AgNPs in presence of Fe^{3+} ions at different pH (B) relative activity (±SD) ($N = 6$) of BSA-alliin AgNPs to detect Fe^{3+} ions (C) changes in the absorbance of BSA-alliin AgNPs (5 mL) in the presence of 25 μM Fe^{3+} at 5 minutes intervals and (D) the first order reaction kinetics model ($N = 8$) (±SD).

© 2026 The Author(s). Published by the Royal Society of Chemistry

Open Access Article. Published on 16 March 2026. Downloaded on 5/23/2026 8:44:04 PM.
This article is licensed under a Creative Commons Attribution-NonCommercial 3.0 Unported Licence.

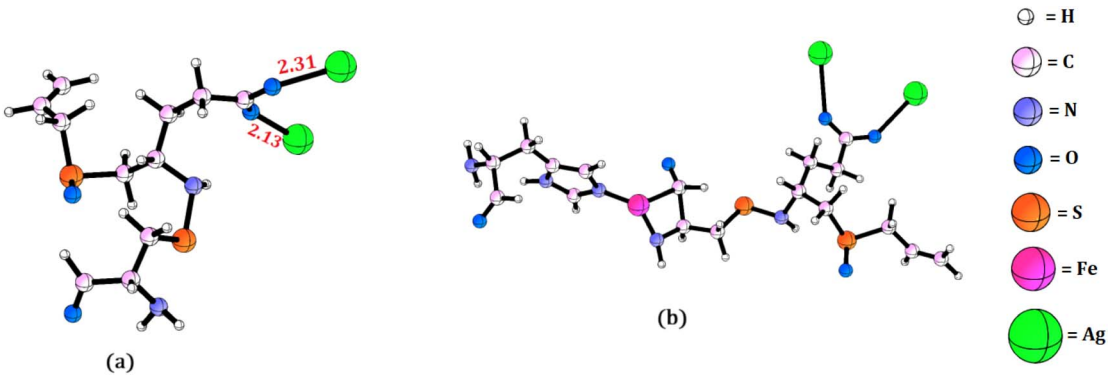

Fig. 6 Optimized geometry of (a) alliin-Ag molecule and (b) Fe^{3+} doped histidine-alliin-Ag molecule.

electrostatic interactions or complexation with Fe^{3+} ions in acidic environments. At lower or higher pH levels, either the nanoparticle stability is compromised or the ion-binding affinity is reduced, leading to decreased sensitivity. Optimal pH conditions are crucial for ensuring reliable and reproducible detection in real-world samples. Previous studies have similarly reported enhanced Fe^{3+} ion detection under slightly acidic pH, which enhances selectivity by minimizing interference from competing metal ions and reducing background absorbance shifts.[25,29,30,59] Thus, pH 4 is established as the optimal condition for Fe^{3+} ion detection using BSA-alliin-AgNPs at room temperature, offering a balance between nanoparticle stability and ion interaction efficiency.

3.6 Kinetics of the reactive interaction between BSA-alliin-AgNPs and Fe^{3+}

UV-visible spectra used to measure the kinetics of the interaction between 25 μl of 1 nM Fe^{3+} ions and 5 mL BSA-alliin-AgNPs showed a gradual decrease in absorbance of Ag NPs over time at room temperature and pH 4. When the experimental data were analyzed using different kinetic models as presented in eqn (2)–(4), the resulting regression fits (R^2 values) were all quite close to each other indicating that each model provided a good mathematical fit to the experimental data. However, the regression fit for zero-order kinetics was marginally higher ($R^2 = 0.959$; $Y = 0.296 - 0.0007X$; A_t *vs.* T) (Fig. 5C and D) than for first- ($R^2 = 0.956$; $Y = 0.002 + 0.998$; $\ln(A_t/A_0)$ *vs.* T) and second-order ($R^2 = 0.952$; $Y = 0.0085X + 3.379$; $1/A_t$ *vs.* T) kinetics. The differences in R^2 values among the models are marginal and may not, by themselves, provide statistically rigorous discrimination of reaction kinetics.

3.7 Possible mechanism

Fig. 6(a) shows the optimized geometry of alliin-Ag molecule where the Ag atoms interact with the –COOH group of alliin molecule. The computed Ag–O distances are 2.13 and 2.31 Å. The calculated binding energy per Ag atom is 19.4 kcal mol^{-1}, indicating that Ag atoms forms strong bonds with O atoms of –COOH group.

Further to investigate the interaction of Fe^{3+} ion with the histidine molecule of bovine serum albumin, we optimized the geometry of Fe^{3+} doped histidine molecule along with the Ag doped alliin (Fig. 6b). The Fe^{3+} ion interacts with NH moiety of histidine and C atom of CHO group. The binding energy is also found to be significant (16.1 kcal mol^{-1}) suggesting that a stable Ag-alliin-Fe complex will be formed.

4. Conclusion

This study provides a unique, eco-friendly, and highly sensitive colorimetric nanosensor for Fe^{3+} ion detection. It uses silver nanoparticles synthesised from garlic-derived alliin and stabilised by bovine serum albumin. The BSA-alliin-AgNPs showed excellent selectivity, a clear colorimetric response, and a surprisingly low detection limit of 5.54 fM. The sensor's performance was optimised at pH 4 and used zero-order reaction kinetics. Computational investigations support the stable interaction of Fe^{3+} with the sensor matrix. The sensor's practical applicability was confirmed with real water samples, indicating its potential for environmental monitoring and on-site iron contamination detection.

Author contributions

RP: conceptualization, investigation, analysis, manuscript preparation. PJT: validation, software, AKG: validation, software, CT: conceptualization, methodology, supervision, visualization, writing – review & editing. All read and approved the final version of the manuscript.

Conflicts of interest

The authors have no conflicts to declare. The authors declare that they have no known competing financial interests or personal relationships that could have appeared to influence the work reported in this paper.

Data availability

The authors confirm that all data supporting the findings of this study are available within the article.

Open Access Article. Published on 16 March 2026. Downloaded on 5/23/2026 8:44:04 PM. This article is licensed under a Creative Commons Attribution-NonCommercial 3.0 Unported Licence.

Acknowledgements

The authors express their sincere appreciation to the Director of CSIR-NEIST (Council of Scientific & Industrial Research-North East Institute of Science and Technology) Jorhat, Assam for the continuous support and valuable suggestions provided throughout the research (Manuscript ref: CSIR-NEIST/PUB/2025/146). The author thanks to Analytical Chemistry Group & SAIF, CSIR-NEIST Jorhat for their instrumental support. The authors thanks to SEED Division, DST New Delhi for financial support (ref no.: DST/SEED/TSP/STI/2022/915).

Notes and references

1 WHO, *Guidelines for Drinking-Water Quality: Fourth Edition Incorporating the First Addendum*, World Health Organization, Geneva, 4th edn, 2017.
2 H. Ye and T. A. Rouault, Human iron-sulfur cluster assembly, cellular iron homeostasis, and disease, *Biochemistry*, 2010, **49**, 4945–4956.
3 M. J. Kotze, D. P. van Velden, S. J. van Rensburg and R. Erasmus, Pathogenic mechanisms underlying iron deficiency and iron overload: New insights for clinical application, *eJIFCC*, 2009, **20**, 108–123.
4 EPA, *Drinking water regulations and contaminants*, U.S. Environmental Protection Agency, https://www.epa.gov/sdwa, (accessed June 2025).
5 J. Briffa, E. Sinagra and R. Blundell, Heavy metal pollution in the environment and their toxicological effects on humans, *Heliyon*, 2020, **6**, e04691.
6 X. Meng, B. Lei, N. Qi and B. Wang, The selective detection of Fe^{3+} ions using citrate-capped gold nanoparticles, *Anal. Biochem.*, 2022, **637**, 114453.
7 K. Ghosh, S. Rathi and R. Kushwaha, Sensing of Fe(III) ion via turn-on fluorescence by fluorescence probes derived from 1-naphthylamine, *Tetrahedron Lett.*, 2013, **54**, 6460–6463.
8 J. Li, Q. Wang, Z. Guo, H. Ma, Y. Zhang, B. Wang, D. Bin and Q. Wei, Highly selective fluorescent chemosensor for detection of Fe^{3+} based on Fe_3O_4@ZnO, *Sci. Rep.*, 2016, **6**, 23558.
9 Y. Du, Y. Li, Y. Liu, N. Liu, Y. Cheng, Q. Shi, X. Liu, Z. Tao, Y. Guo, J. Zhang, N. Askaria and H. Li, Stalk-derived carbon dots as nanosensors for Fe^{3+} ions detection and biological cell imaging, *Front. Bioeng. Biotechnol.*, 2023, **11**, 1187632.
10 Y. Zhang, Y. Chen, H. Jiang and X. Wang, Selective and sensitive detection of Fe^{3+} ion in drinking water using L-glutathione stabilized red fluorescent gold nanoclusters, *J. Nanosci. Nanotechnol.*, 2016, **16**, 12179–12186.
11 H. Ye, L. Zhao, X. Ren, Y. Cai and H. Chi, "Switch-off-on" detection of Fe^{3+} and F^- ions based on fluorescence silicon nanoparticles and their application to food samples, *Nanomaterials*, 2022, **12**, 213.
12 S. Kang, H. Han, K. Lee and K. M. Kim, Ultrasensitive detection of Fe^{3+} ions using functionalized graphene quantum dots fabricated by a one-step pulsed laser ablation process, *ACS Omega*, 2022, **7**, 2074–2081.
13 Z. Liu, N. Li, P. Liu, Z. Qin and T. Jiao, Highly sensitive detection of iron ions in aqueous solutions using fluorescent chitosan nanoparticles functionalized by rhodamine B, *ACS Omega*, 2022, **7**, 5570–5577.
14 M. Golshan, B. Gheitarani, S.-A. Safavi-Mirmahalleh and M. Salami-Kalajahi, Rhodamine B-modified nanocrystalline cellulose as fluorescent sensor for Fe^{3+} ion detection, *Macromol. Mater. Eng.*, 2025, **310**, 2400285.
15 M. Shellaiah, K. W. Sun, K. Anandan, M. Bhushan, A. Murugan and W. T. Li, Biocompatible rhodamine functionalized nanodiamond for heavy metal ions detection: Demonstration by paper strips, cellular imaging, and real water investigations, *Diam. Relat. Mater.*, 2025, **158**, 112698.
16 P. Rajam and R. Mahalakshmy, An effective colorimetric and fluorescent chemosensor derived from modified curcumin for the detection of the Fe^{3+} ion, *Indian J. Chem.*, 2023, **62**, 518–526.
17 A. Bellingeri, F. Bertela, L. Burratti, A. Calantropio, C. Battocchio, P. Lupetti, E. Paccagnini, G. Iucci, M. Marsotto, P. Prosposito, I. Corsi and I. Venditti, Detection of Fe(III) ion based on bifunctionalized silver nanoparticles: Sensitivity, selectivity and environmental safety, *Mater. Chem. Phys.*, 2024, **313**, 128671.
18 D. Uzunoğlu, M. Ergüt, C. G. Kodaman and A. Özer, Biosynthesized silver nanoparticles for colorimetric detection of Fe^{3+} ions, *Arabian J. Sci. Eng.*, 2024, **49**, 7783–7794.
19 Z. M. Ma, X. S. Wu, D. D. Zheng, J. Y. Wei, Y. N. Xie, Y. B. Shi, K. Huang, X. M. Zhang and J. Liu, Well-Aligned TiO_2 nanotube arrays with Ag nanoparticles for highly efficient detection of Fe^{3+} ion, *Nanoscale Res. Lett.*, 2019, **14**, 49.
20 D. R. Yuniarni, N. I. Pratiwi, A. Umar and C. Imawan, Synthesis of silver nanoparticles (AgNPs) using Sodium chloride (NaCl) for Iron (III) ions detection based on colorimetric and optical changes, *J. Phys.: Conf. Ser.*, 2020, **1528**, 012062.
21 A. Ebrahimi, F. Samari, E. Eftekhar and S. Yousefinejad, Rapid and efficient colorimetric sensing of clindamycin and Fe^{3+} using controllable phyto-synthesized silver/silver chloride nanoparticles by *Syzygium cumini* fruit extract, *J. Anal. Sci. Technol.*, 2022, **13**, 10.
22 J. Tashkhourian and O. Sheydaei, Chitosan capped silver nanoparticles as colorimetric sensor for the determination of iron(III), *Anal. Bioanal. Chem. Res.*, 2017, **4**, 249–260.
23 X. Gao, Y. Lu, S. He, X. Li and W. Chen, Colorimetric detection of iron ions (III) based on the highly sensitive plasmonic response of the N-acetyl-L-cysteine-stabilized silver nanoparticles, *Anal. Chim. Acta*, 2015, **879**, 118–125.
24 K.-P. T. Dang, T.-G. Nguyen, T.-D. Cao, V.-D. Le, C.-H. Dang, N. P. H. Duy, P. T. T. Phuong, D. M. Huy, T. T. K. Chi and T.-D. Nguyen, Biogenic fabrication of a gold nanoparticle sensor for detection of Fe^{3+} ions using a smartphone and machine learning, *RSC Adv.*, 2024, **14**, 20466.

© 2026 The Author(s). Published by the Royal Society of Chemistry

Open Access Article. Published on 16 March 2026. Downloaded on 5/23/2026 8:44:04 PM. This article is licensed under a Creative Commons Attribution-NonCommercial 3.0 Unported Licence.

25 K. Kim, Y.-S. Nam, Y. Lee and K.-B. Lee, Highly sensitive colorimetric assay for determining Fe^{3+} based on gold nanoparticles conjugated with glycol chitosan, *J. Anal. Methods Chem.*, 2017, 3648564.
26 A. S. Andreani, E. S. Kunarti, T. Hashimoto, T. Hayashita and S. J. Santosa, Fast and selective colorimetric detection of Fe^{3+} based on gold nanoparticles capped with ortho-hydroxybenzoic acid, *J. Environ. Chem. Eng.*, 2021, **9**, 105962.
27 M. R. Bindhu and M. Umadevi, Green synthesized gold nanoparticles as a probe for the detection of Fe^{3+} ions in water, *J. Cluster Sci.*, 2014, **25**, 969–978, DOI: 10.1007/s10876-013-0679-8.
28 N. S. Komova, K. V. Serebrennikova, A. N. Berlina, S. M. Pridvorova, A. V. Zherdev and B. B. Dzantiev, Gold nanoparticles functionalized with mercaptosuccinic acid as a means for detecting Fe(III) ions, *Chem. Proc.*, 2021, **5**, 6.
29 W. Ji, Z. Zhu, S. Dong, J. Nie and B. Du, Optical detection of Fe^{3+} ions in aqueous solution with high selectivity and sensitivity by using sulfasalazine functionalized microgels, *Sensors*, 2019, **19**, 4223.
30 N. A. Zulkefli and W. E. F. W. Khalid, Spectrophotometric detection of Fe^{3+} ion based on alizarin red S (ARS) reagent, *Malays. J. Chem.*, 2024, **26**, 320–329.
31 G. Singh, Sushma, Priyanka, Pawan, P. Satija, Shilpy, G. Kaur, J. Singh and J. Singh, Colorimetric detection of Fe^{3+} ions using Schiff base-chalcone functionalized bis(1,2,3-triazolyl-γ-propyltriethoxysilanes), *Inorg. Chim. Acta*, 2021, **527**, 120576.
32 S. Sen, T. Singh, J. Im, D. Debnath and G. Biswas, *Terminalia chebula*: a novel natural product colorimetric sensor for Fe^{2+} and Fe^{3+} ions, *J. Anal. Sci. Technol.*, 2022, **13**, 39, DOI: 10.1186/s40543-022-00348-z.
33 K. Dayanidhi and N. K. Eusuff, Distinctive detection of Fe^{2+} and Fe^{3+} by biosurfactant capped silver nanoparticles via naked eye colorimetric sensing, *New J. Chem.*, 2021, **45**, 9936–9943.
34 A. Meher, A. Tandi, S. Moharana, S. Chakroborty, S. S. Mohapatra, A. Mondal, S. Dey and P. Chandra, Silver nanoparticle for biomedical applications: A review, *Hybrid Adv.*, 2024, **6**, 100184.
35 M. Acuña, M. Walter, M. Paez and M. I. Azocar, Colorimetric detection of bovine serum albumin (BSA protein) by interaction and modification of silver nanoparticles, *ACS Omega*, 2025, **10**, 2679–2687.
36 R. Paw, M. Hazarika, P. K. Boruah, A. J. Kalita, A. K. Guha, M. R. Das and C. Tamuly, Highly sensitive and selective colorimetric detection of dual metal ions (Hg^{2+} and Sn^{2+}) in water: an eco-friendly approach, *RSC Adv.*, 2021, **11**, 14700–14709.
37 A. Alnehia, A. B. Al-Odayni, A. H. Al-Hammadi, S. A. Alramadhan, H. Alnahari, W. S. Saeed and A. Al-Sharabi, Garlic extract-mediated synthesis of ZnS nanoparticles: Structural, optical, antibacterial, and hemolysis studies, *J. Nanomater.*, 2023, 8200912.
38 International Council for Harmonisation of Technical Requirements for Pharmaceuticals for Human Use, *ICH Q2(R2) Guideline on Validation of Analytical Procedures: Test and Methodology*, European Medicines Agency, European Union, Netherlands, 2023.
39 R. Painuli, S. Raghav and D. Kumar, Selective interactions of Al(III) with plasmonic AgNPs by colorimetric, kinetic, and thermodynamic studies, *ACS Omega*, 2019, **4**, 3635–3645.
40 Y. Zhao and D. G. Truhlar, The M06 suite of density functionals for main group thermochemistry, thermochemical kinetics, noncovalent interactions, excited states, and transition elements: two new functionals and systematic testing of four M06-class functionals and 12 other functionals, *Theor. Chem. Acc.*, 2008, **120**, 215–241.
41 M. J. Frisch, G. W. Trucks, H. B. Schlegel, G. E. Scuseria, *et al.*, *Gaussian 16, Revision A.03*, Gaussian, Inc., Wallingford, CT, 2016.
42 A. Dhaka, S. C. Mali, S. Sharma and R. Trivedi, A review on biological synthesis of silver nanoparticles and their potential applications, *Results Chem.*, 2023, **6**, 101108.
43 T. C. Prathna, N. Chandrasekaran, A. M. Raichur and A. Mukherjee, Biomimetic synthesis of silver nanoparticles by *Citrus limon* (lemon) aqueous extract and theoretical prediction of particle size, *Colloids Surf., B*, 2011, **82**, 152–159.
44 S. H. Omar and N. A. Al-Wabel, Organosulfur compounds and possible mechanism of garlic in cancer, *Saudi Pharm. J.*, 2010, **18**, 51–58.
45 A. Shang, S.-Y. Cao, X.-Y. Xu, R.-Y. Gan, G.-Y. Tang, H. Corke, V. Mavumengwana and H.-B. Li, Bioactive compounds and biological functions of garlic (*Allium sativum* L.), *Foods*, 2019, **8**, 246.
46 K. B. Narayanan and N. Sakthivel, Biological synthesis of metal nanoparticles by microbes, *Adv. Colloid Interface Sci.*, 2010, **156**, 1–13.
47 S. Iravani, Green synthesis of metal nanoparticles using plants, *Green Chem.*, 2011, **13**, 2638–2650.
48 B. Zewde, O. Atoyebi, A. Gugssa, K. J. Gaskell and D. Raghavan, An investigation of the interaction between bovine serum albumin-conjugated silver nanoparticles and the hydrogel in hydrogel nanocomposites, *ACS Omega*, 2021, **6**, 11614–11627.
49 A. Gebregeorgis, C. Bhan, O. Wilson and D. Raghavan, Characterization of silver/bovine serum albumin (Ag/BSA) nanoparticles structure: morphological, compositional, and interaction studies, *J. Colloid Interface Sci.*, 2013, **389**, 31–41.
50 M. Rai, A. Yadav and A. Gade, Silver nanoparticles as a new generation of antimicrobials, *Biotechnol. Adv.*, 2009, **27**, 76–83.
51 G. H. Major, J. W. Pinder, D. E. Austin, D. R. Baer, *et al.*, Perspective on improving the quality of surface and material data analysis in the scientific literature with a focus on x-ray photoelectron spectroscopy (XPS), *J. Vac. Sci. Technol., A*, 2023, **41**, 038501.
52 S. Ravi, S. Zhang, Y. R. Lee, K. K. Kang, J. M. Kim, J. W. Ahn and W. S. Ahn, EDTA-functionalized KCC-1 and KIT-6 mesoporous silicas for Nd^{3+} ion recovery from aqueous solutions, *J. Ind. Eng. Chem.*, 2018, **67**, 210–218.

Open Access Article. Published on 16 March 2026. Downloaded on 5/23/2026 8:44:04 PM.
This article is licensed under a Creative Commons Attribution-NonCommercial 3.0 Unported Licence.

53 J. Zhang, M. Zhang, H. Wan, J. Zhou and A. Lu, Coordinatively stiffen and toughen polymeric gels via the synergy of crystal-domain cross-linking and chelation cross-linking, *Nat. Commun.*, 2025, **16**, 320.

54 P. G. Kshirsagar, V. De Matteis, S. Pal and S. S. Sangaru, Silver–gold alloy nanoparticles (AgAu NPs): Photochemical synthesis of novel biocompatible, bimetallic alloy nanoparticles and study of their in vitro peroxidase nanozyme activity, *Nanomaterials*, 2023, **13**, 2471.

55 J. Guo, R. Zhong, W. Li, Y. Liu, Z. Bai, J. Yin, J. Liu, P. Gong, X. Zhao and F. Zhang, Interaction study on bovine serum albumin physically binding to silver nanoparticles: Evolution from discrete conjugates to protein coronas, *Appl. Surf. Sci.*, 2015, **359**, 82–88.

56 Y. Li, Z. Cui, L. Huang, D. Zhang, Y. Shen, J. Cheng and J. Wang, Aggregation-based analytical chemistry in point-of-care nanosensors, *Aggregate*, 2024, **5**, e559.

57 L. Rozenberga, W. Skinner, D. G. Lancaster, W. M. Bloch, A. Blencowe, M. Krasowska and D. A. Beattie, A europium metal–organic framework for dual Fe^{3+} ion and pH sensing, *Sci. Rep.*, 2022, **12**, 11982.

58 S.-P. Wu, Y.-P. Chen and Y.-M. Sung, Colorimetric detection of Fe^{3+} ions using pyrophosphate functionalized gold nanoparticles, *Analyst*, 2011, **136**, 1887.

59 N. Azizi-Khereshki, H. Z. Mousavi, M. Farsadrooh, M. Evazalipour, M. Feizi-Dehnayebi, G. M. Ziarani, M. Henary, S. Rtimi and T. M. Aminabhavi, Biogenic synthesis of silver nanoparticles for colorimetric detection of Fe^{3+} in environmental samples: DFT calculations and molecular docking studies, *J. Environ. Manage.*, 2025, **387**, 125880.

© 2026 The Author(s). Published by the Royal Society of Chemistry